


Article

The Rotating Flow of Magneto Hydrodynamic Carbon Nanotubes over a Stretching Sheet with the Impact of Non-Linear Thermal Radiation and Heat Generation/Absorption

Sher Muhammad ^{1,2}, Gohar Ali ¹, Zahir Shah ^{3,4,*} , Saeed Islam ³ and Syed Asif Hussain ^{1,2}¹ Department of Mathematics, Islamia College, Peshawar 25000, KP, Pakistan;

shermphil123@gmail.com (S.M.); gohar.ali@icp.edu.pk (G.A.); asif@cecos.edu.pk (S.A.H.)

² Department of Mathematics, Cecos University of Information Technology & Emerging Science, Peshawar 25000, KP, Pakistan³ Department of Mathematics, Abdul Wali Khan University, Mardan 23200, KP, Pakistan; saeedislam@awkum.edu.pk⁴ Gandhara Institute of Science & Technology, South Canal Road, Peshawar 25000, KP, Pakistan

* Correspondence: zahir1987@gist.edu.pk; Tel.: +92-333-9198-823

Received: 13 February 2018; Accepted: 19 March 2018; Published: 22 March 2018



Abstract: The aim of this research work is to investigate the innovative concept of magnetohydrodynamic (MHD) three-dimensional rotational flow of nanoparticles (single-walled carbon nanotubes and multi-walled carbon nanotubes). This flow occurs in the presence of non-linear thermal radiation along with heat generation or absorption based on the Casson fluid model over a stretching sheet. Three common types of liquids (water, engine oil, and kerosene oil) are proposed as a base liquid for these carbon nanotubes (CNTs). The formulation of the problem is based upon the basic equation of the Casson fluid model to describe the non-Newtonian behavior. By implementing the suitable non-dimensional conditions, the model system of equations is altered to provide an appropriate non-dimensional nature. The extremely productive Homotopy Asymptotic Method (HAM) is developed to solve the model equations for velocity and temperature distributions, and a graphical presentation is provided. The influences of conspicuous physical variables on the velocity and temperature distributions are described and discussed using graphs. Moreover, skin fraction coefficient and heat transfer rate (Nusselt number) are tabulated for several values of relevant variables. For ease of comprehension, physical representations of embedded parameters such as radiation parameter (Rd), magnetic parameter (M), rotation parameter (K), Prandtl number (Pr), Biot number (λ), and heat generation or absorption parameter (Q_h) are plotted and deliberated graphically.

Keywords: Single-Walled Carbon Nanotube (SWCNT); Multi-Walled Carbon Nanotube (MWCNT); MHD; Casson model; stretching sheet; non-linear thermal radiation; HAM

1. Introduction

Single-walled carbon nanotubes (SWCNTs) and multi-walled carbon nanotubes (MWCNTs) are similar in certain aspects, but they also have some striking differences. SWCNTs are an allotrope of sp^2 hybridized carbon, and are similar to fullerenes. Single-walled carbon nanotubes (SWCNTs) have unique character due to their unusual structure. The structure of SWCNTs demonstrates significant optical and electronic features, tremendous strength and flexibility, and high thermal and chemical stability. As a result, SWCNTs are expected to dramatically impact several industries, particularly

with respect to electronic displays, health care, and composites. MCWNTs are also suitable for many applications due to their high conductivity. Applications include electrostatic discharge protection in wafer processing and fabrication, plastic components for automobiles, plastics rendered conductive to enable the electrostatic spray painting of automobile body parts. The carbon nanotube (CNT) is composed of allotropes of carbon, and has a cylinder-shaped nanostructure. The molecules of carbon in cylindrical form have remarkable physiognomies that are useful for applied sciences, optics, physical sciences, fabric sciences, energy, health sciences, and manufacturing [1]. Terminology with respect to carbon nanotubes (CNTs) was first presented by Iijima [2] in 1991, who explored multi-walled carbon nanotubes (MWCNTs) using the Kratschmer and Huffman technique. Single-walled carbon nanotubes (SWCNTs) were reported by Donald Bethune in 1993 [3]. It is acknowledged that nanofluids will reduce the difficulties connected with materials with low thermal conductivities, like coal oil, water, engine oil, gasoline etc. Nanofluids contain a homogeneous combination of nano-size materials, with lengths ranging from 1 nm to 100 nm in a base liquid. Nanofluids have applications in automobile engine freezing, heat interchangers, solar heating water, bio-medicine, cooling of micro-electronic chips, and enhanced productivity of diesel engines. Expressions with respect to nanofluids were initially presented by Choi [4] using the inconsistent thermal conductivity of liquid (water) by depositing copper nanomaterial. Said et al. [5] reported that the SWCNT nano-liquids improve the thermal performance of solar collectors in place of water, in a context where one of the most manageable and contamination-free source of renewable energy is solar energy, and solar aerials. It can transform solar radiation into heat energy. In the textile industry, much attention has been paid to coating CNTs because of their uses in the sound industry, for example in megaphones and headsets. Xiao et al. [6] reported that very thin CNT films radiate lurid sound, and therefore prepared thin film CNT megaphones. Halelfadel et al. [7] examined the productivity of water-based nanofluid CNTs and deliberated the consequences of stumpy volume fraction nanoparticles in a range from 0.0055% to 0.278% on the physical properties (density, viscosity, thermal conductivity, and specific heat) of nanofluids. Aman et al. [8] investigated the influence of magnetohydrodynamics on Poiseuille flow and heat analysis of CNTs with a Casson fluid vertical channel. Further studies on carbon nanotubes can be appraised in [9–14].

Hayat et al. [15] investigated the three-dimensional (3D) rotating flow of carbon nanotubes with a Darcy–Frochheimer porous medium. Manevitch et al. [16] studied nonlinear optical vibrations of single-walled carbon nanotubes. Imtiaz et al. [17] discussed the convective flow of carbon nanotubes between rotating stretchable disks with thermal radiation effects in his research article. In an article by Tran et al. [18] the purification and dissolution of carbon nanotube fiber spun using the floating catalyst method were reported.

In applied sciences and engineering, flows with respect to nonlinear materials are essential. To explore the properties of stream and heat analysis, a number of rheological models are available for second-, third-, and fourth-grade fluid, micro polar fluid, Jaffery fluid, and Maxwell fluid models. One such type of general model is the Casson model [19] presented to calculate the flow behaviors and display yield stress. When the produced stress is greater than the shear stress, the Casson fluid acts similarly to a solid. Examples of these (Casson) fluids are chocolate, honey, blood, jelly, tomato sauce, and soup. Dash et al. [20] studied the performances of Casson liquids over a permeable medium restricted by a circular cylinder. Pramanik [21] inspected the impact of radiation on the Casson liquid stream and heat through a porous extending medium. Hassan et al. [22] investigated the unsteady Casson fluid layer and Newtonian heat through an oscillating surface. Asma et al. [23] examined the magnetohydrodynamic (MHD) unsteady flow of Casson fluid over an oscillating plate fixed in porous media. Walicka and Falicki [24] studied the influence of Reynold number on the stream of Casson liquid. Nadeem et al. [25] deliberated three-dimensional flows with convective boundary conditions of a Casson fluid. Specific studies related to Casson liquid flow can be found in [26,27].

The flow behavior is profoundly affected by the strength and placement of applied magnetic field. The applied magnetic field affects the deferred nanoparticles and reforms their absorption inside the fluid, which substantially modifies the flow features of heat analysis. The analysis of

magnetohydrodynamic (MHD) flow of an electrically directing liquid flow has several major uses in engineering fields, such as in atomic reactor freezing, magnetohydrodynamic power producers, plasma studies, and the petroleum industry. Arial [28] studied the impact of MHDs on the two-dimensional (2D) flow of a gummy liquid imposing normal to the plane, and analyzed the influence of the Hartmann number. Ganapathirao and Ravindran [29] investigated the suction/injunction effect on 2D MHD steady flow with the chemical reaction along with mixed convection. Rahman et al. [30] and Srinivasacharya et al. [31] deliberated the impression of heat generation/absorption on 2D nanofluid flow and reported that the Nusselt number was enhanced with large values of the Biot number and the slip parameter. Hameed et al. [32] investigated the combined magnetohydrodynamic and electric field effect on an unsteady Maxwell nanofluid flow over a stretching surface under the influence of variable heat and thermal radiation. Recently, Shah et al. [33,34] studied the effects of hall current on three dimensional non-Newtonian nanofluids and micropolar nanofluids in a rotating frame.

In various engineering processes, the boundary film stream on a stretching/extending sheet is of great importance. In metallurgical and polymer productions, stretching is a significant phenomenon in the construction of polymer sheets, food processing, film coating, and drawing of copper wire. Crane [35] is the pioneering author who introduced the fluid flow by means of the stretching sheet. The work of Crane was expanded upon by many scholars, like Vajraelu and Roper [36] who investigated the stream of second-grade fluids and stretching sheets. Rosca and Pop [37] and Sajid et al. [38] deliberated the vicious unsteady motion due to a shrinking/stretching curved medium. Further research on the liquid stream due to the stretching sheet can be found in several studies [39,40]. Similarly the thermal radiation is significant in certain applications where radiant discharge depends on temperature and nanoparticle volume fraction. Pooya et al. [41] performed a thermal exploration of single phase nanofluid flow. Afify et al. [42] considered the impact of thermal radiation on 2D boundary layer flow. Brinkman [43] has investigated the viscosity of concentrated suspensions and solution. Xue [44] has discussed the model for thermal conductivity of CNTs based composites.

Here, the main aim is to deal the heat generation/absorption along with thermal radiation in a steady MHD 3D rotational stream of a Casson nanofluid with an entirely different base liquid. The movement of liquid is created by means of a stretching sheet. Two classes of carbon nanotubes (CNTs), specifically single-walled carbon nanotubes (SWCNTs) and multiple-walled carbon nanotubes (MWCNTs), are employed to explore the behavior of nanofluids. The acceptable transformation implies alterations the system of partial differential equations (PDEs) to a mandatory system of ordinary differential equations (ODEs).

The Homotopy Asymptotic Method (HAM) [45–48] involves calculation expansion for velocities and the energy profile. Here, the expressions of velocities and temperature are mathematically and graphically examined. Furthermore, the coefficient of skin friction and Nusselt number are explored numerically, and the results are discussed graphically.

2. Problem Formulation

We assume a three-dimensional, viscous, steady, MHD rotating Casson nanofluid flow comprising single- and multi-walled CNTs over a stretching sheet. The flows of SWCNTs and MWCNTs are taken under the influence of non-linear thermal radiation and heat absorption/generation. We adopt the coordinate structure in such a manner that the surface associated with the xy -plane and fluid is placed in $z > 0$. The stretching rate of the surface and the angular velocity of fluid are assumed as $c > 0$ and Ω , respectively. The surface temperature is a result of the convective heating process, which involves the hot fluid temperature T_f and coefficient of heat transfer h_f . The geometry of the problem shown in Figure 1.

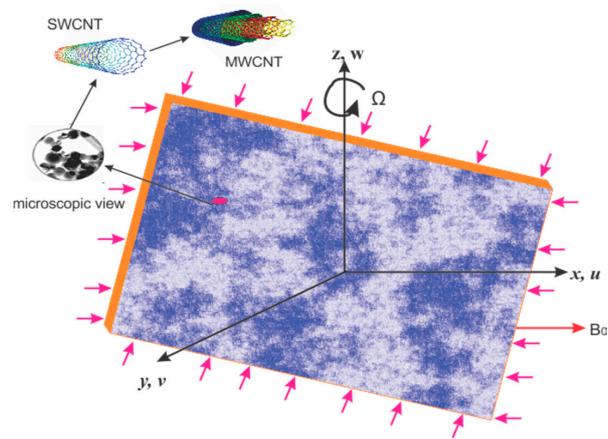


Figure 1. Schematic physical geometry.

The necessary constitutive model of a Casson fluid [19,22,24] is as follows:

$$\begin{aligned} \frac{\tau_{mn}^{c.f}}{2e_{mn}} &= \mu_{\gamma}^{c.f} + \frac{p_y}{\sqrt{2\pi_d}}; & \pi_d > \pi_{c.f}, \\ \frac{\tau_{mn}^{c.f}}{2e_{mn}} &= \mu_{\gamma}^{c.f} + \frac{p_y}{\sqrt{2\pi_{c.f}}}; & \pi_d < \pi_{c.f}. \end{aligned} \tag{1}$$

where $\tau_{mn}^{c.f}$ is the shear stress tensor of the Casson fluid, $\mu_{\gamma}^{c.f}$ is the Casson fluid plastic viscosity, π_d is the rate of deformation, and $\pi_{c.f}$ is the critical amount of current product that depends on the Casson fluid. We assume a situation in which a certain liquid requires the gradual growth of the the shear stress to sustain the constant rate of strain. In the case $\pi_d > \pi_{c.f}$ the Casson fluid possesses the kinematic viscosity $v^{c.f}$ as a function of $\mu_{\gamma}^{c.f}$, $\rho^{c.f}$, and Casson parameter β , such that

$$\begin{aligned} \mu^{c.f} &= \mu_{\gamma}^{c.f} + \frac{p_y}{\sqrt{2\pi_d}}, \quad p_y = \frac{\mu_{\gamma}^{c.f} \sqrt{2\pi_d}}{\beta}, \quad v^{c.f} = \frac{\mu^{c.f}}{\rho^{c.f}}, \\ v^{c.f} &= \frac{\mu^{c.f} \left(1 + \frac{1}{\beta}\right)}{\rho^{c.f}}, \quad \frac{\partial \tau^{c.f}}{\partial z} = \left(1 + \frac{1}{\beta}\right) u_{zz}. \end{aligned} \tag{2}$$

Here $\mu^{c.f}$ represents the dynamic viscosity of the Casson fluid, $\beta = \frac{\mu_{\gamma}^{c.f} \sqrt{2\pi_d}}{p_y}$, and p_y shows the yield stress of the liquid. From the denotation of β describing the ratio of the product of $\mu_{\gamma}^{c.f}$ and $\sqrt{2\pi_d}$ to the yield stress p_y , it can be seen that the resistivity in liquid is greater if $\beta > 0$, and the liquid presents an inviscid behavior if $\beta < 0$, which eliminates the viscosity of the Casson fluid.

Taking into account the above declared rules, the primary equation takes the following form [8,25]:

$$u_x + v_y + w_z = 0, \tag{3}$$

$$\rho_{nf} \{u u_x + v u_y + w u_z - 2\Omega v\} = \mu_{nf} \left(1 + \frac{1}{\beta}\right) (u_{zz}) - \sigma_{nf} B_0^2 (u), \tag{4}$$

$$\rho_{nf} \{v v_x + v v_y + w v_z - 2\Omega u\} = \mu_{nf} \left(1 + \frac{1}{\beta}\right) (v_{zz}) - \sigma_{nf} B_0^2 (v), \tag{5}$$

$$u T_x + v T_y + w T_z = \alpha_{nf} (T_{zz}) - \frac{(q_z^{red})}{(\rho c_p)_f} + \frac{Q_0(T - T_0)}{(\rho c_p)_f}. \tag{6}$$

The allied boundary conditions [25] are defined as

$$\begin{aligned} u_w = c x, v = 0, w = 0, -k_{nf} T_z = h_f (T_f - T) \text{ at } z = 0, \\ u = v = w = 0, T = T_\infty, \text{ at } z = \infty. \end{aligned} \tag{7}$$

where u, v and w specify velocities in the x, y, z directions, respectively, ρ_{nf} represents the nanofluid density, μ_{nf} the nanofluid dynamic viscosity, and σ_{nf} the electrical conductivity of the nanofluid. T shows the local temperature, k_{nf} is the nanofluid thermal conductivity, and $(\rho c_p)_{nf}$ is the nanofluid specific heat capacity.

Brinkman [43] defined the dynamic viscosity of nano-liquid in term of base liquid as:

$$\mu_{nf} = \frac{\mu_f}{(1 - \phi)^{2.5}}. \tag{8}$$

The density, specific heat capacity, and rate of thermal conductivities of the nanofluid [7,8] are expressed as:

$$\begin{aligned} \rho_{nf} &= \rho_f(1 - \phi) + \phi \rho_{CNT}, \mu_{nf} = \frac{\mu_f}{(1 - \phi)^{2.5}}, \\ \alpha_{nf} &= \frac{\mu_f}{(\rho c_p)_{nf}}, (\rho C_p)_{nf} = (1 - \phi)(\rho C_p)_f + \phi(\rho C_p)_{CNT}, \\ \sigma_{nf} &= \sigma_f \left(\frac{1 + 3(\sigma - 1)\phi}{(\sigma + 2) - (\sigma - 1)\phi} \right). \end{aligned} \tag{9}$$

Here, the model by Xue [44] is implemented to calculate the thermal conductivities

$$\frac{k_{nf}}{k_f} = \frac{1 - \phi + 2\phi \left(\frac{k_{CNT}}{k_{CNT} - k_f} \ln \left(\frac{k_{CNT} + k_f}{2 k_f} \right) \right)}{1 - \phi + 2\phi \left(\frac{k_f}{k_{CNT} - k_f} \ln \left(\frac{k_{CNT} + k_f}{2 k_f} \right) \right)}. \tag{10}$$

where ρ_{CNT} shows the density of carbon nanotube, $(\rho c_p)_{CNT}$ denotes the specific heat of the carbon nanotube, and $\rho_f, (\rho c_p)_f$ represent the density and specific heat of base fluid, respectively.

$q^{rad} = -\frac{4\sigma^*}{3k^*} \frac{\partial T^4}{\partial z}$ has been achieved using the Roseland approximation [43], where σ^* is the Stefan Boltzmann constant, and k^* is the absorption coefficient. We can observe that temperature difference in liquid motion is suitably negligible, so T^4 can be expressed in linear form using the Taylor's series, neglecting the higher terms: $T^4 = 4T_\infty^3 - 3T_\infty^4$. Therefore, we have $q^{rad} = -\frac{16\sigma^*}{3k^*} T^3 \frac{\partial T}{\partial z}$.

Using the following suitable similarities variable [13],

$$\begin{aligned} u = c x f'(\eta), v = c x g(\eta), w = -\sqrt{c v_f} f(\eta), \\ \Theta(\eta) = T_\infty + (T_f - T_\infty)\Theta(\eta), \eta = \left[\frac{c}{v_f} \right]^{\frac{1}{2}}. \end{aligned} \tag{11}$$

Equation (3) is verified identically and Equations (4)–(10) take the following system when we use the similarities variables:

$$\left(1 + \frac{1}{\beta} \right) f'''(\eta) - \zeta_1 \zeta_2 [f(\eta) f''(\eta) + (f'(\eta))^2 + 2K g(\eta) - \zeta_4 M f'(\eta)] = 0, \tag{12}$$

$$\left(1 + \frac{1}{\beta} \right) g''(\eta) - \zeta_1 \zeta_2 [f(\eta) g'(\eta) + f'(\eta) g(\eta) - 2K f'(\eta) - \zeta_4 M g(\eta)] = 0, \tag{13}$$

$$\frac{d}{d\eta} \left(\zeta_5 + \frac{4}{3} Rd [1 + (\Theta(\eta) - 1)\Theta(\eta)]^3 \right) \Theta'(\eta) + \zeta_3 Pr [f(\eta)\Theta'(\eta) + Q_h \Theta(\eta)], \tag{14}$$

$$\begin{aligned} f(\eta) = g(\eta) = 0, f'(\eta) = 1, \Theta'(\eta) = \frac{k_f}{k_{nf}} (1 - \Theta(\eta))\lambda, \text{ at } \eta = 0, \\ f'(\eta) = g(\eta) = \Theta(\eta) = 0, \text{ at } \eta = \infty. \end{aligned} \tag{15}$$

Here K represent the rotation parameter, M represents the magnetic parameter, Pr represents the Prandtl number, Q_h denotes the heat generation or absorption parameter, Rd represents radiation parameter, and λ is the Biot number, and are expressed as follows:

$$K = \frac{\Omega}{c}, M = \frac{\sigma_f B_0^2 g}{c}, Pr = \frac{(\rho c_p)_f}{k_f}, Q_h = \frac{Q}{c(\rho c_p)_f}, Rd = \frac{4\sigma^* T_\infty^3}{3k^* k_f}, \lambda = \frac{h_f}{k_f} \sqrt{\frac{v_f}{c}}. \tag{16}$$

$$\begin{aligned} \zeta_1 &= (1 - \varphi)^{2.5}, \zeta_2 = \left\{ (1 - \varphi) + \frac{\rho_{CNT}\varphi}{\rho_f} \right\}, \zeta_3 = \left[(1 - \varphi) + \frac{(\rho c_p)_{CNT}}{(\rho c_p)_f} \right], \\ \zeta_4 &= \sigma_f \left(\frac{1+3(\sigma-1)\varphi}{(\sigma+2)-(\sigma-1)\varphi} \right), \zeta_5 = \frac{k_{nf}}{k_f} = \frac{1-\varphi + \left(2 \frac{k_{CNT}}{k_{CNT}-k_f} \ln \frac{k_{CNT}+k_f}{2k_f} \right) \varphi}{1-\varphi + \left(2 \frac{k_f}{k_{CNT}-k_f} \ln \frac{k_{CNT}+k_f}{2k_f} \right) \varphi}. \end{aligned} \tag{17}$$

3. Physical Quantities of Interest

The physical quantities of interest such as Skin friction C_f is defined as $C_f = \left(1 + \frac{1}{\beta}\right) \frac{\mu_{nf}}{\rho_f u_w^2} (u_y)_{y=0}$ and local Nusselt number Nu_x , is defined as $Nu_x = \frac{x k_{nf}}{k_f (T_w - T_\infty)} (T_y)_{y=0}$, the dimensionless forms of these main design quantities are as follows:

$$\tilde{C}_{fx} = \frac{1}{(1 - \varphi)^{2.5}} \left(1 + \frac{1}{\beta}\right) f''(0), \tilde{C}_{fy} = \frac{1}{(1 - \varphi)^{2.5}} \left(1 + \frac{1}{\beta}\right) g'(0), Nu = -\frac{k_{nf}}{k_f} \Theta'(0). \tag{18}$$

4. Solution Methodology

In this section, the system of coupled nonlinear differential Equations (12)–(14), along with specific boundary conditions (Equation (15)) are solved analytically by using the Homotopy Analysis Method (HAM). The idea of the HAM was first presented by Liao [44,45] using the concept of homotopy. For solution development, the HAM scheme has certain advantages, such as the fact that it is free from small or large emerging parameters. The HAM offers an easy way to confirm the convergence of solution, and it provides liberty in terms of the right selection of the base function and the auxiliary parameter.

In the HAM scheme, the assisting parameter h is used to regulate and control the convergence of the solutions. The initial estimates are:

$$f_0(\eta) = 1 - e^{-x}, g_0(\eta) = e^{-x}, \Theta_0(\eta) = \frac{k_f \gamma}{k_f \gamma k_{nf}} e^{-x}. \tag{19}$$

The linear operators L are as follows:

$$L_f(f) = f_{\eta\eta\eta}, \quad L_g(g) = g_{\eta\eta}, \quad L_\Theta(\Theta) = \Theta_{\eta\eta}. \tag{20}$$

For the above stated differential operators, constants are shown as:

$$\begin{aligned} L_f(C_1 + C_2\eta + C_3\eta^2) &= 0, \\ L_g(C_4 + C_5\eta) &= 0, \\ L_\Theta(C_6 + C_7\eta) &= 0. \end{aligned} \tag{21}$$

4.1. Zeroth Order Deformation of the Problem

$U \in [0, 1]$ is an embedded parameter with auxiliary parameters h_f, h_g and h_Θ . The problem deforms for the zero order as follows:

$$(1 - U)L_g(f(\eta, U) - f_0(\eta)) = Uh_f N_f \{f(\eta, U), g(\eta, U)\}, \tag{22}$$

$$(1 - U)L_g(g(\eta, U) - g_0(\eta)) = U h_g N_g \{f(\eta, U), g(\eta, U)\}, \tag{23}$$

$$(1 - U) L_\Theta(\Theta(\eta, U) - \Theta_0(\eta)) = U h_\Theta N_\Theta \{f(\eta, U), g(\eta, U), \Theta(\eta, U)\}. \tag{24}$$

The specific boundary conditions are obtained as:

$$\begin{aligned} f(0, U) = f'(0, U) = g(0, U) = \Theta(0, U) = 0, \\ f(1, U) = f'(1, U) = g(1, U) = \Theta(1, U) = 0. \end{aligned} \tag{25}$$

The resultant nonlinear operators are:

$$N_f(f(\eta; U), g(\eta; U)) = \left(1 + \frac{1}{\beta}\right) f_{\eta\eta\eta}(\eta; U) + \zeta_1 \zeta_2 [\{f_{\eta\eta}(\eta; U)\}^2 + f(\eta; U) f_{\eta\eta}(\eta; U) + 2K g(\eta; U) - \zeta_4 M f_{\eta}(\eta; U)], \tag{26}$$

$$N_g(g(\eta; U), f(\eta; U)) = \left(1 + \frac{1}{\beta}\right) g_{\eta\eta}(\eta; U) - \zeta_1 \zeta_2 [f_{\eta}(\eta; U) g(\eta; U) + \{f(\eta; U) g_{\eta}(\eta; U)\} - 2K f_{\eta}(\eta; U) - \zeta_4 M g(\eta; U)], \tag{27}$$

$$N_\Theta(\Theta(\eta; U), f(\eta; U)) = \frac{d}{d\eta} \left(\zeta_5 + \frac{4}{3} Rd[1 + (\Theta(\eta) - 1)\Theta(\eta)]^3\right) \Theta_{\eta}(\eta; U) + Pr \zeta_3 [\{f(\eta; U)\} \Theta_{\eta}(\eta; U)] + Q_h \Theta(\eta; U). \tag{28}$$

Taylor’s series expresses $f(\eta; U)$, $g(\eta; U)$ and $\Theta(\eta; U)$. In terms of U we have:

$$\begin{aligned} f(\eta, U) &= f_0(\eta) + \sum_{i=1}^{\infty} f_i(\eta), \\ g(\eta, U) &= g_0(\eta) + \sum_{i=1}^{\infty} g_i(\eta), \\ \Theta(\eta, U) &= \Theta_0(\eta) + \sum_{i=1}^{\infty} \Theta_i(\eta). \end{aligned} \tag{29}$$

where

$$f_i(\eta) = \frac{1}{i!} \{f_{\eta}(\eta, U)\} \Big|_{U=0}, \quad g_i(\eta) = \frac{1}{i!} \{g_{\eta}(\eta, U)\} \Big|_{U=0}, \quad \Theta_i(\eta) = \frac{1}{i!} \{\Theta_{\eta}(\eta, U)\} \Big|_{U=0} \tag{30}$$

4.2. *i*th-Order Deformation Problem

Now we differentiate the zeroth component equations *i*th time to achieve the *i*th order deformation equations with respect to U , so we get:

$$\begin{aligned} L_f(f_i(\eta) - \zeta_i f_{i-1}(\eta)) &= h_f \left(R_i^f(\eta)\right), \\ L_g(g_i(\eta) - \zeta_i g_{i-1}(\eta)) &= h_g \left(R_i^g(\eta)\right), \\ L_\Theta(\Theta_i(\eta) - \zeta_i \Theta_{i-1}(\eta)) &= h_\Theta \left(R_i^\Theta(\eta)\right). \end{aligned} \tag{31}$$

The resultant boundary conditions are:

$$\begin{aligned} f_i = f'_i = g_i = \Theta_i = 0, \quad \text{at } \eta = 0, \\ f_i = f'_i = g_i = \Theta_i = 0 \quad \text{at } \eta = 1. \end{aligned} \tag{32}$$

$$\begin{aligned} R_i^f(\eta) &= \frac{d^3 f_{i-1}}{d\eta^3} + \zeta_1 \zeta_2 \left[\left(\sum_{j=0}^{i-1} \frac{d^2 f_{i-1}}{d\eta^2} \right)^2 + \left(\sum_{j=0}^{i-1} (f_{i-1-j}) \frac{d^2 f_j}{d\eta^2} \right) \right. \\ &\quad \left. + 2K g_{i-1} - \zeta_4 M \left(\sum_{j=0}^{i-1} \frac{d f_{i-1}}{d\eta} \right) \right], \end{aligned} \tag{33}$$

$$R_i^f(\eta) = \frac{d^2 g_{i-1}}{d\eta^2} + \zeta_1 \zeta_2 \left[\left(\sum_{j=0}^{i-1} \frac{df_{i-1}}{d\eta} g_j \right) + \left(\sum_{j=0}^{i-1} f_{i-1-j} \frac{dg_j}{d\eta} \right) - \zeta_4 M g_{i-1} - 2K \left(\sum_{j=0}^{i-1} \frac{df_{i-1}}{d\eta} \right) \right], \quad (34)$$

$$R_i^f(\eta) = \frac{d}{d\eta} \left(\zeta + \frac{4}{3} Rd [1 + (\Theta(\eta) - 1)\Theta(\eta)]^3 \right) \frac{d\Theta_{i-1}}{d\eta} + Pr \zeta_3 \left[\sum_{j=0}^{i-1} f_{i-1-j} \frac{d\Theta_j}{d\eta} + Q_h \sum_{j=0}^{i-1} \Theta_{i-1-j} \right]. \quad (35)$$

where

$$\zeta_i = \begin{cases} 1, & \text{if } U > 1 \\ 0, & \text{if } U \leq 1. \end{cases} \quad (36)$$

5. HAM Scheme Convergence

When we compute the series solutions of the velocity and temperature functions to use the HAM, the assisting parameters h_f , h_g , and h_Θ appear. These assisting parameters are responsible for adjusting the convergence of these solutions. In the possible region of velocities and temperature profiles, $f''(0)$, $g'(0)$, and $\Theta'(0)$ for the 15th-order approximation are plotted, for different values of the embedding parameter. The \hbar -curves consecutively display the valid region.

6. Results and Discussion

The present research has been carried out in order to study magnetohydrodynamics in the three-dimensional rotational flow of nanoparticles (single- and multi-walled carbon nanotubes) in the existence of non-linear thermal radiation along with heat generation or absorption based on the Casson fluid model over a stretching sheet. In this subsection we examine the physical outcomes of dissimilar embedded parameters with respect to the velocity distributions $f'(\eta)$, $g(\eta)$ and temperature distribution $\Theta(\eta)$. The influence of specific model quantities, such as K, M, Pr, Q_h, Rd , and λ (the rotation parameter, magnetic parameter, P and tl number, heat generation or absorption parameter, radiation parameter, and Biot number, respectively) on $f'(\eta)$, $g(\eta)$, and $\Theta(\eta)$ for SWCNTs and MWCNTs as nanoparticles is highlighted in the present discussion. Figure 1 shows the schematic flow geometry of the problem. Figures 2 and 3 present the convergence and probable choice of h-curve for $f''(0)$, $\Theta'(0)$ and $g'(0)$. The effects of model values such as $K, M, Pr, Q_h, Rd, \lambda$ on $f'(\eta)$, $g(\eta)$ and $\Theta(\eta)$ are illustrated in Figures 4–14 and consequence are considered. Figure 4 demonstrates the consequence of rotation parameter K on the velocity profile $f'(\eta)$ for SWCNTs and MWCNTs. The increasing values of K depreciate the value of $f'(\eta)$ and result in a thinner boundary coating for SWCNTs and MWCNTs. Physically, when the value of rotation parameter K enlarges, the rate of rotation becomes dominant as compared to the stretching rate. Hence, there is a larger effect of rotation parameter K delivering resistance to the fluid stream. For the maximum value of the rotation parameter K , the values of velocity-filled $f'(\eta)$ become small near the boundary, and the layer becomes thinner, so the x-coordinate of velocity component is a decreasing function of the rotation parameter K . The similar impact for the high value of magnetic parameter M is shown in Figure 5 for both CNTs. It is obvious from the sketch that an increment in the magnetic parameter M depreciates the value of $f'(\eta)$. Usually, high values of magnetic parameter M improve the contradictory force (friction force), known as the Lorentz force. The corresponding force has the propensity to condense the value of $f'(\eta)$. The influence of volume fraction of nanoparticle φ on the velocity profile $f'(\eta)$ is exhibited in Figure 6 for SWCNTs and MWCNTs. We observe that increment in $f'(\eta)$ increases the quantity of φ for SWCNTs and MWCNTs. In fact, adding the nanoparticle φ enhances the energy and cohesive force between the atoms of the liquid, causing it to become frail and halt the faster liquid. Figure 7 illustrates the behavior of the Casson fluid parameter β on $f'(\eta)$ for SWCNTs and MWCNTs. With increasing values of the Casson fluid parameter β decreases the velocity field $f'(\eta)$ in the boundary layer. It is noted that to increases the value of the Casson fluid parameter β implies a reduction in the yield stress of the Casson liquid, and hence there is a clear acceleration in the motion of the boundary layer stream neighboring the

stretching surface of the sheet. Moreover, it has been found that Casson fluids are similar to Newtonian fluids for large values of $\beta \rightarrow \infty$. The impact of nanoparticle volume fraction φ on $g(\eta)$ has been illustrated in Figure 8 for SWCNTs and MWCNTs. It is observed that the large value of φ decreases the transverse velocity $g(\eta)$ for SWCNTs and MWCNTs. In Figure 9 the velocity distribution $g(\eta)$ is intended for various values of rotation K . It is demonstrated that K has an energetic character in accelerating the flow in the y-plane. The suitably bulky value of K corresponds to an oscillatory pattern close to the wall of the sheet for SWCNTs and MWCNTs. The core reason is that the sheet is extended only along the x-plane, and due to rotation the liquid flow is solely possible in the y-direction. It can be observed that a high value of K reduces the magnitude of $g(\eta)$. Figure 10 shows that the features of the magnetic parameter M on $g(\eta)$ are qualitatively equivalent to those of K . Generally, the large value of M improves the resistance to the motion of liquid, which depreciates the value of $g(\eta)$. In Figure 11 it can be seen that the increment in Pr generates a fall in temperature $\Theta(\eta)$ due to the weaker thermal diffusivity. Physically, thermal layer thickness and $\Theta(\eta)$ form the reducing function of Pr . For the high Pr , the fluid retains low thermal conductivities, which causes the thinner thermal boundary layer. Consequently, the heat rate is increased. The fluids which have a small Pr possess excellent thermal conductivity. Figure 12 presents the impact of radiation parameter Rd on $\Theta(\eta)$ for SWCNTs and MWCNTs as nanoparticles. It seems that the increase in Rd boosts $\Theta(\eta)$, which is associated to the thickness of the boundary film. Basically, high Rd delivers more heat to functional nanofluids, which indicates an increment in $\Theta(\eta)$ in the presence of SWCNTs and MWCNTs. Figure 13 characterizes the temperature field $\Theta(\eta)$ for heat generation parameter Q_h . The value of $\Theta(\eta)$ and the thermal thickness of boundary layer are improved for a large value of Q_h . In this manner, the rate of heat is enhanced as the Q_h value is increased. Consequently, we note that the thermal thickness of boundary film is a function of Q_h .

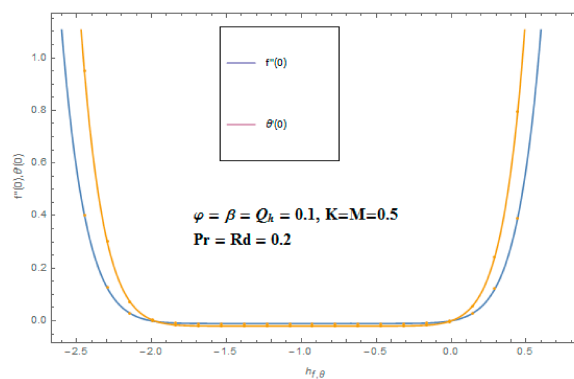


Figure 2. The combined h-curves of the velocity and heat profile with a 15-order approximation.

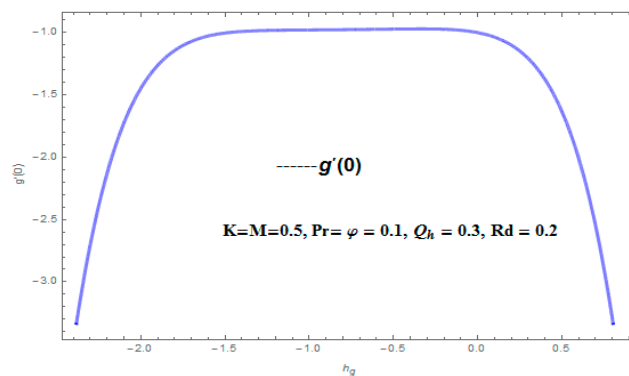


Figure 3. The h-curves of velocity $g(\eta)$ with a 15-order approximation.

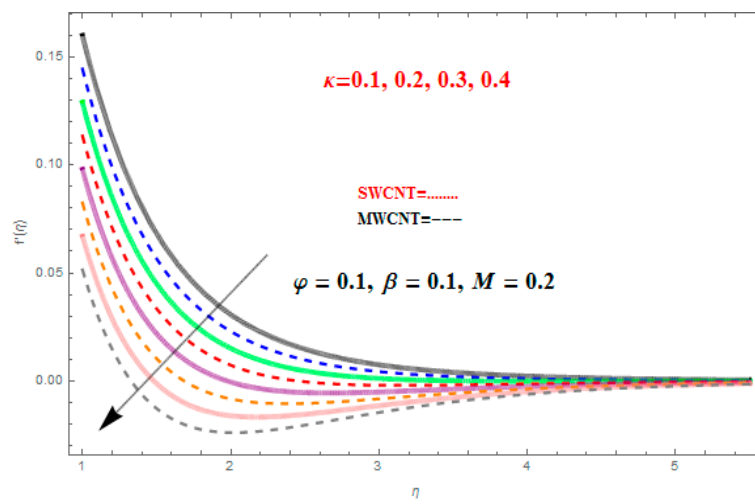


Figure 4. Effect of the rotation parameter K on $f'(\eta)$.

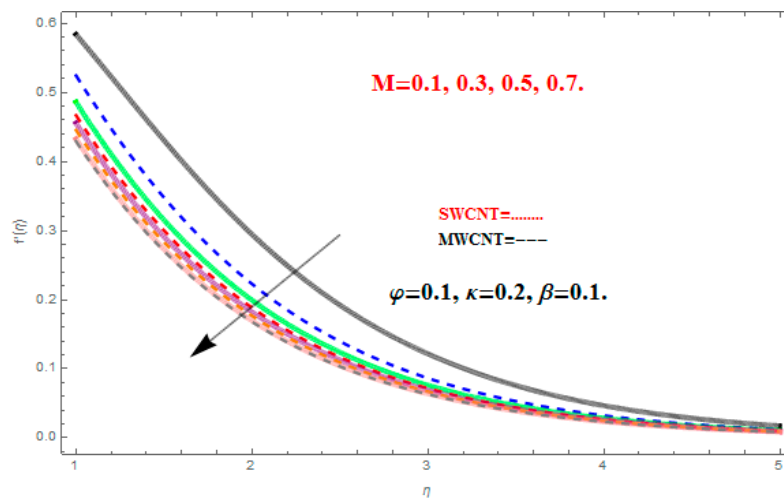


Figure 5. Effect of the magnetic parameter M on $f'(\eta)$.

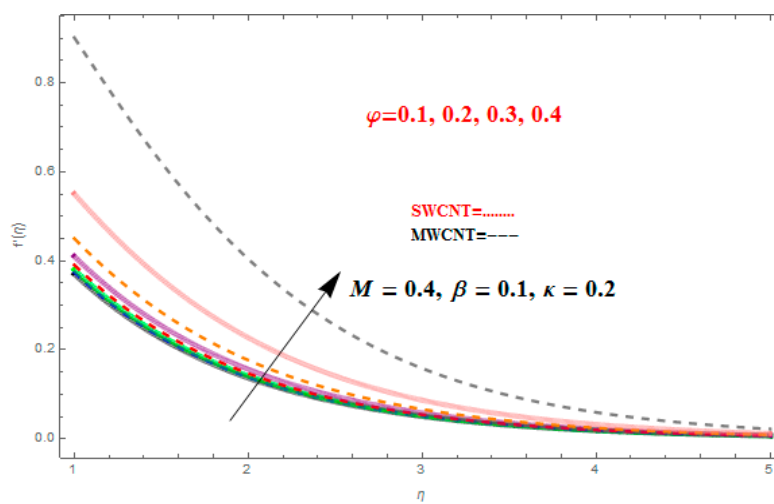


Figure 6. Effect of the volume fraction of the nanoparticle parameter φ on $f'(\eta)$.

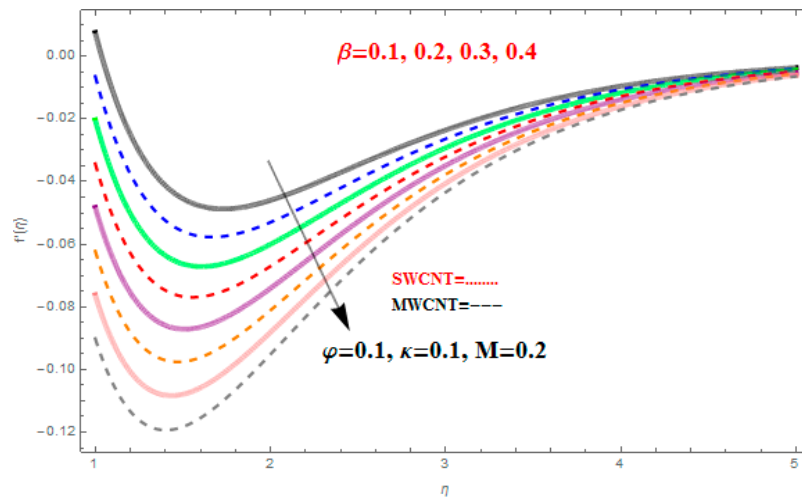


Figure 7. Effect of the Casson parameter β on $f'(\eta)$.

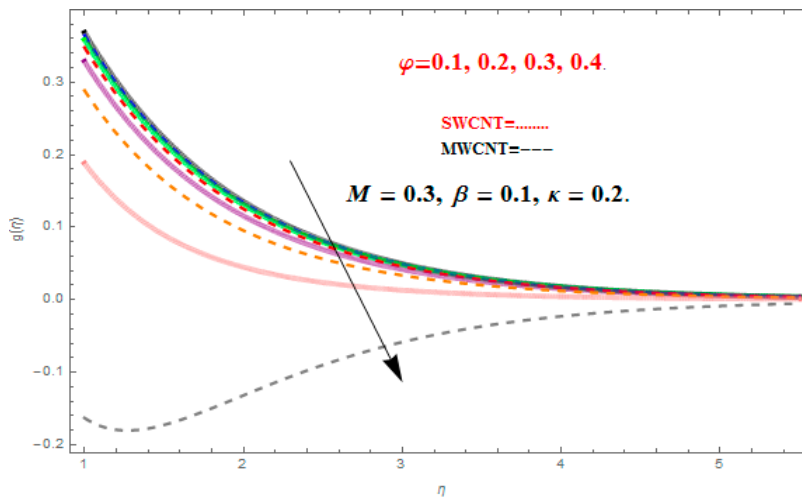


Figure 8. Effect of the volume fraction parameter φ on the velocity field $g(\eta)$.

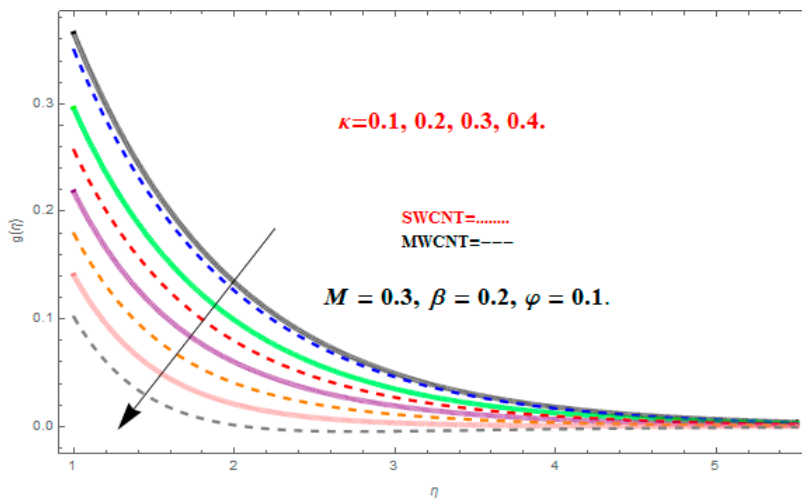


Figure 9. Effect of the rotation parameter K on the velocity field $g(\eta)$.

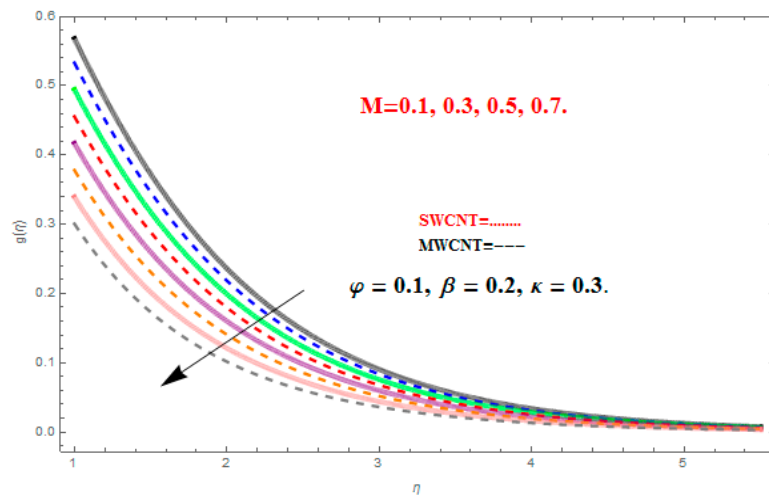


Figure 10. Effect of the magnetic parameter M on the velocity field $g(\eta)$.

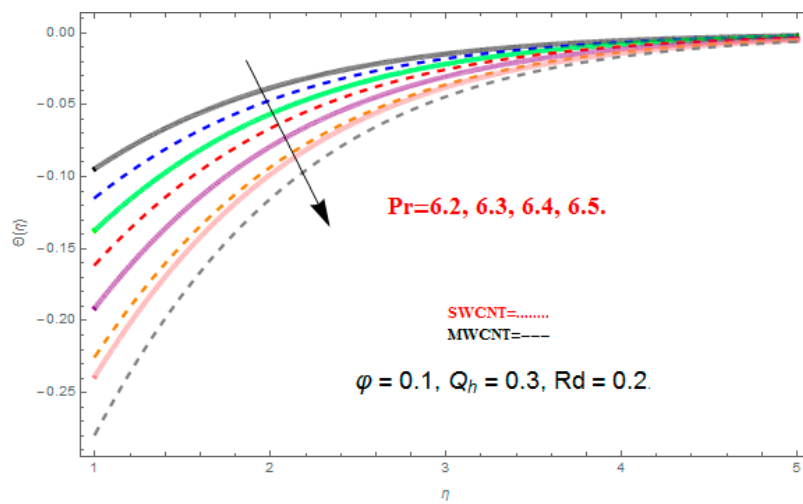


Figure 11. Effect of the Prandtl number Pr on the temperature field $\Theta(\eta)$.

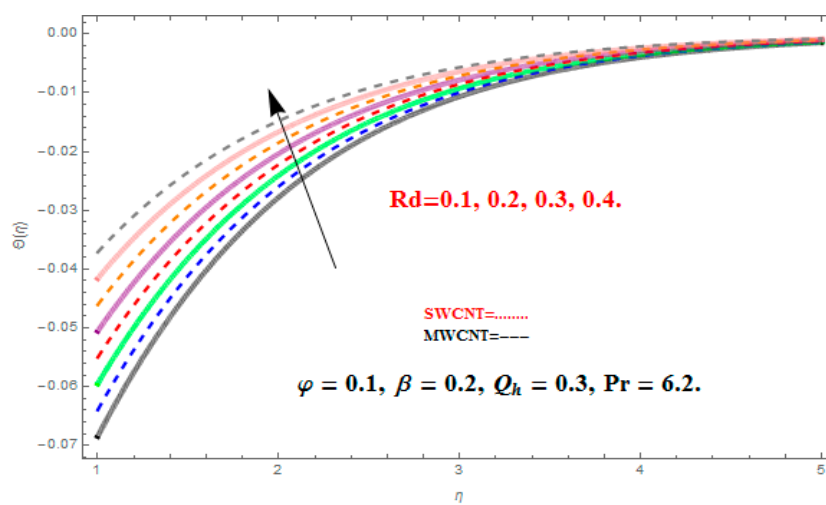


Figure 12. Effect of the radiation parameter Rd on the temperature field $\Theta(\eta)$.

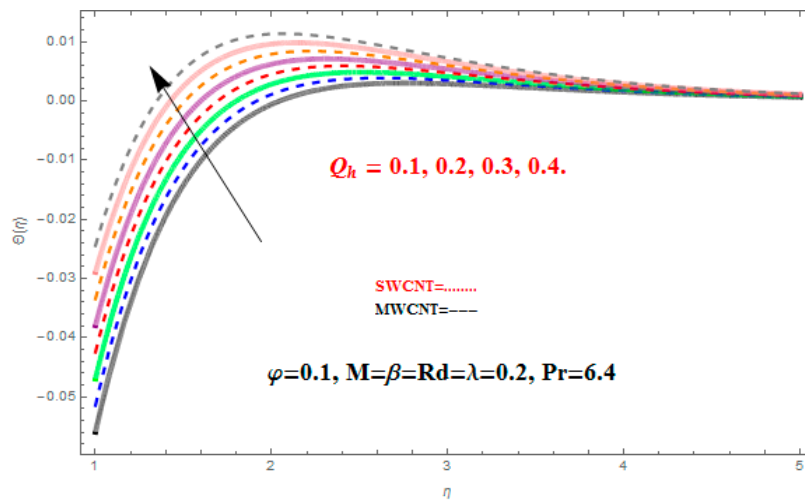


Figure 13. Effect of the heat generation/absorption parameter Q_h on the temperature field $\Theta(\eta)$.

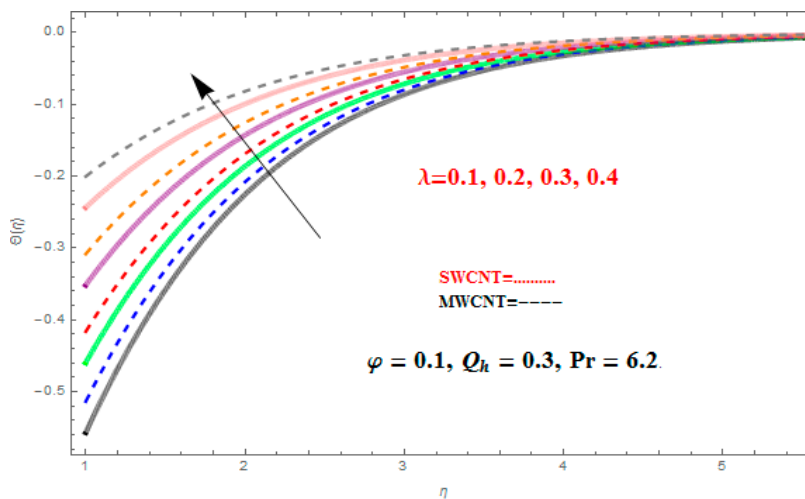


Figure 14. Effect of the Biot number λ on the temperature field $\Theta(\eta)$.

Variation in $\Theta(\eta)$ due to the Biot number λ is represented in the Figure 14 for both CNTs. The stronger value of λ leads to an enhanced temperature field $\Theta(\eta)$ and a thickness of the thermal film that allows the thermal impact to infiltrate deeper into the dormant liquid. In fact, λ depends on the heat transfer coefficient h_f , which is maximum for a massive value of λ , illustrating an increase in temperature.

Table Discussion

Table 1 illustrates various physical properties of certain base liquids (water, kerosene oil and engine oil) and nanoparticles such as SWCNTs and MWCNTs. Xue [44] calculated dissimilar values of effective thermal conductivities of CNT nanofluids for several values of the volume fraction ϕ of the CNTs shown in Table 2. It can be seen in Table 2 that the thermal conductivity is improved with inspiring volume fraction ϕ of CNTs. For the same values of ϕ , can be noted that the nanofluids with SWCNTs have higher effective thermal conductivities as compared to those with MWCNTs. The logic for this is the elevated value of thermal conductivity of SWCNTs ($6600 \text{ Wm}^{-1}/\text{k}^{-1}$) as opposed to MWCNTs ($3000 \text{ Wm}^{-1}/\text{k}^{-1}$), as given in Table 1.

Table 1. The thermo physical properties of carbon nanotubes (CNTs) of some base fluids. SWCNT: single-walled carbon nanotube; MWCNT: multi-walled carbon nanotube

Physical Properties		Density $\rho(\text{kg/m}^3)$	Thermal Conduct $k(\text{W/mk})$	Specific Heat $c_p(\text{kg}^{-1}/\text{k}^{-1})$
Base fluid	Water	997	0.613	4197
	Kerosene (lamp) oil	783	0.145	2090
	Engine oil	884	0.144	1910
Nanoparticles	SWCNT	2600	6600	425
	MWCNT	1600	3000	796

Table 2. Thermal conductivity values of CNTs with different volume fraction values.

Volume Fraction φ	Thermal Conductivity k_{nf} for SWCNT	Thermal Conductivity k_{nf} for MWCNT
0	0.145	0.145
0.01	0.174	0.172
0.02	0.204	0.2
0.03	0.235	0.228
0.04	0.266	0.257

Physical values such as the skin friction co-efficient (C_f) and the Nusselt number (Nu) for the engineering purposes are calculated through Tables 3 and 4, respectively. Table 3 presents the numerical values of skin friction (C_{fx}) and (C_{fy}). It can be observed that the large values of M , φ and β increase the skin friction (C_{fx}) and (C_{fy}) of both SWCNTs and MWCNTs, where the large value of K reduces the skin friction (C_{fx}) of both SWCNTs and MWCNTs and increases skin friction along the y-axis (C_{fy}). Table 4 presents the numerical results of the Nusselt number (Nu). It can be noted that the large values of M and K increase the (Nu) of both SWCNTs and MWCNTs, where the large values of λ , Rd and Q_h reduce the Nusselt number of both SWCNTs and MWCNTs.

Table 3. Numerical data of the skin-friction coefficient for dissimilar values of M , K , φ , and β .

M	K	φ	β	$-C_{fx}$		$-C_{fy}$	
				SWCNT	MWCNT	SWCNT	MWCNT
0.0	0.1	0.1	0.1	1.08611	1.03456	1.24004	1.14526
0.1				1.15356	1.12677	1.27582	1.19870
0.3				1.19726	1.14340	1.34626	1.24358
0.1	0.0			1.19564	1.04566	1.19564	1.13657
	0.3			0.98477	0.23561	1.44063	1.17452
	0.5			0.85341	0.02537	1.61105	1.32435
	0.1	0.0		0.96929	0.23409	1.10111	1.03452
		0.3		1.54113	1.45473	1.23251	1.10034
		0.5		1.68492	1.52435	1.69792	1.37342
		0.1	0.1	1.69211	1.57235	1.72340	1.22349
			0.3	1.73421	1.62345	1.88191	1.31902
			0.5	1.92345	1.81189	1.90823	1.59321

Table 4. Numerical data of Nusselt numbers for dissimilar values of M , K , λ , Rd , and Q_h when $Pr = 6.4$.

M	K	λ	Rd	Q_h	Nu_x	
					SWCNT	MWCNT
0.0	0.1	0.1	0.1	0.1	0.116964	0.231567
0.1					0.116974	0.232390
0.3					0.116988	0.233321
0.1	0.0				0.116965	0.134136
	0.3				0.116966	0.134342
	0.5				0.116967	0.134351
	0.1	0.3			0.116953	0.261532
		0.5			0.116943	0.261531
		0.8			0.116926	0.261530
		0.1	0.5		0.118451	0.156382
			1.0		0.120623	0.234521
			1.5		0.122502	0.267373
			0.1	0.5	0.116945	0.234536
				1.0	0.116928	0.198342
				1.5	0.116895	0.162435

7. Conclusions

We address the three-dimensional rotational flow of Casson fluids containing carbon nanotubes (SWCNTs and MWCNTs) as nanoparticles in the presence of thermal radiation along with heat generation over a stretching sheet. The effects of embedded parameters are observed and studied graphically. Moreover, the variation of the skin friction, Nusselt number, and their influences on the velocity and heat distributions are examined. The main points of the present study are shown below:

- For CNTs, large values of K (the rotation parameter) produce smaller velocities $f'(\eta)$ and $g(\eta)$, but the opposite tendency is detected for temperature profile $\Theta(\eta)$.
- Increasing the nanoparticle volume fraction φ into the working liquid boosted $f'(\eta)$, $g(\eta)$ and $\Theta(\eta)$ values for SWCNTs and MWCNTs.
- A strong magnetic parameter M reduces $f'(\eta)$ and $g(\eta)$, while increases the temperature $\Theta(\eta)$.
- The thermal layer rises through heat generation for SWCNTs and MWCNTs.
- The large values of Prandlt number Pr , reduces nanoparticle temperature $\Theta(\eta)$.
- Large values of Biot number λ boost temperature and thicken the boundary film concentration.
- The degree of coefficient of skin friction increases for larger φ values. The results show that skin friction in case of SWCNTs is higher than in MWCNTs.
- Heat transfer rate is controlled by large values of λ and Pr .
- Nusselt number is greater with SWCNTs as opposed to MWCNTs.

Acknowledgments: The authors are thankful to the anonymous reviewers and the Editor-in-Chief for the productive comments that led to positive enhancement in the paper.

Author Contributions: S.M. and Z.S. modelled and solved the problem. S.M. and G.A. wrote the manuscript. G.A. and S.I. thoroughly checked the mathematical modeling and English language corrections. S.I. and S.A.H. contributed in the results and discussions. All the corresponding authors finalized the manuscript after its internal evaluation.

Conflicts of Interest: The author declares that they have no competing interests.

References

1. Dai, L.; Chang, D.W.; Baek, J.B.; Lu, W. Carbon nanomaterials for advanced energy conversion and storage. *Small* **2012**, *8*, 1130–1166. [[PubMed](#)]
2. Iijima, S. Helical microtubules of graphitic carbon. *Nature* **1991**, *354*, 56–58. [[CrossRef](#)]
3. Ajayan, P.M.; Iijima, S. Capillarity-induced filling of carbon nanotubes. *Nature* **1993**, *361*, 333–334. [[CrossRef](#)]

4. Choi, S.U.S. *Enhancing Thermal Conductivity of Fluids with Nanoparticles, Developments and Applications of Non-Newtonian Flows*; Siginer, D.A., Wang, H.P., Eds.; American Society of Mechanical Engineers (ASME): New York, NY, USA, 1995; Volume 231, pp. 99–105.
5. Said, Z.; Saidur, R.; Rahim, N.A.; Alim, M.A. Analyses of energy efficiency and pumping power for a conventional flat plate solar collector using SWCNTs based nanofluid. *Energy Build.* **2014**, *78*, 1–9. [[CrossRef](#)]
6. Xiao, J.; Pan, X.; Guo, S.; Ren, P.; Bao, X. Toward fundamentals of confined catalysis in carbon nanotube. *J. Am. Chem. Soc.* **2015**, *137*, 477–480. [[CrossRef](#)] [[PubMed](#)]
7. Halefadi, S.; Mare, T.; Estelle, P. Efficiency of carbon nanotubes water based nanofluids as coolants. *Exp. Therm. Fluid Sci.* **2014**, *53*, 104–110. [[CrossRef](#)]
8. Aman, S.; Khan, I.; Ismail, Z.; Salleh, M.Z.; Alshomrani, A.S.; Alghamdi, M.S. Magnetic field effect on Poiseuille flow and heat transfer of carbon nanotubes along a vertical channel filled with Casson fluid Citation. *AIP Adv.* **2017**, *7*, 015036. [[CrossRef](#)]
9. Hayat, T.; Hussain, Z.; Alsaedi, A.; Asghar, S. Carbon nanotubes effects in the stagnation point flow towards a nonlinear stretching sheet with variable thickness. *Adv. Powder Technol.* **2016**, *27*, 1677–1688. [[CrossRef](#)]
10. Wen, D.; Ding, Y. Effective thermal conductivity of aqueous suspensions of carbon nanotubes. *J. Thermophys. Heat Transf.* **2004**, *18*, 481–485. [[CrossRef](#)]
11. Mayer, J.; Mckrell, T.; Grote, K. The influence of multi-walled carbon nanotubes on single-phase heat transfer and pressure drop characteristics in the transitional flow regime of smooth tubes. *Int. J. Heat Mass Transf.* **2013**, *58*, 597–609. [[CrossRef](#)]
12. Kamli, R.; Binesh, A. Numerical investigation of heat transfer enhancement using carbon nanotube-based non-newtonian nanofluids. *Int. Commun. Heat Mass Transf.* **2010**, *37*, 1153–1157. [[CrossRef](#)]
13. Hussain, S.T.; Haq, R.U.; Khan, Z.H.; Nadeem, S. Water driven flow of carbon nanotubes in a rotating channel. *J. Mol. Liq.* **2016**, *214*, 136–144. [[CrossRef](#)]
14. Aman, S.; Khan, I.; Ismail, Z.; Salleh, M.Z.; Al-Mdallal, Q.M. Heat transfer enhancement in free convection flow of CNTs Maxwell nanofluids with four different types of molecular liquids. *Sci. Rep.* **2017**, *7*, 1–13. [[CrossRef](#)] [[PubMed](#)]
15. Hayat, T.; Haider, F.; Muhammad, T.; Alsaedi, A. Three Dimensional rotating flow of carbon nanotubes with Darcy-Frochheimer porous medium. *PLoS ONE* **2017**, *12*, e0179576. [[CrossRef](#)] [[PubMed](#)]
16. Manevitch, L.I.; Smirnov, V.V.; Strozzi, M.; Pellicano, F. Nonlinear optical vibrations of single-walled carbon nanotubes. *Int. J. Nonlinear Mech.* **2017**, *94*, 351–361. [[CrossRef](#)]
17. Imtiaz, M.; Hayat, T.; Alsaedi, A.; Ahmad, B. Convective flow of carbon nanotubes between rotating stretchable disks with thermal radiation effects. *Int. J. Heat Mass Transf.* **2016**, *101*, 948–957. [[CrossRef](#)]
18. Tran, T.Q.; Headrick, R.J.; Bengio, E.A.; Myint, S.M.; Khoshnevis, H.; Jamali, V.; Duong, H.M.; Pasquali, M. Purification and Dissolution of carbon nanotube fiber SPUM from floating catalyst method. *ACS Appl. Mater. Interfaces* **2017**, *9*, 37112–37119. [[CrossRef](#)] [[PubMed](#)]
19. Casson, N. *A Flow Equation for Pigment Oil Suspensions of the Printing Ink Type, Rheology of Disperse Systems*; Pergamon Press: New York, NY, USA, 1959; pp. 84–104.
20. Dash, R.K.; Mehta, K.N.; Jayaraman, G. Effect of yield stress on the flow of a Casson fluid in a homogeneous porous medium bounded by a circular tube. *Appl. Sci. Res.* **1996**, *57*, 133–149. [[CrossRef](#)]
21. Pramanik, S. Casson fluid flow and heat transfer past an exponentially porous stretching surface in presence of thermal radiation. *Ain Shams Eng. J.* **2014**, *5*, 205–212. [[CrossRef](#)]
22. Hussanan, A.; Salleh, M.Z.; Tahar, R.M.; Khan, I. Unsteady boundary layer flow and heat transfer of a Casson fluid past an oscillating vertical plate with Newtonian heating. *PLoS ONE* **2014**, *9*, e108763. [[CrossRef](#)] [[PubMed](#)]
23. Asma, K.; Khan, I.; Arshad, K.; Sharidan, S. Unsteady MHD free convection flow of Casson fluid past over an oscillatin vertical plate embedded in a porous medium. *Eng. Sci. Technol. Int. J.* **2015**, *18*, 309–317.
24. Walicka, A.; Falicki, J. Reynolds number effects in the flow of an electro rheological fluid of Casson type between fixed surface of revolution. *Appl. Math. Comput.* **2015**, *250*, 639–649.
25. Nadeem, S.; Haq, R.U.; Noreen, A.S. MHD three-dimensional boundary layer flow of Casson nanofluid past a linearly stretching sheet with convective boundary condition. *IEEE Trans. Nanotechnol.* **2014**, *13*, 109–115. [[CrossRef](#)]
26. Mukhopadhyay, S.; Bhattacharyya, K.; Hayat, T. Exact solutions for the flow of Casson fluid over a stretching surface with transpiration and heat transfer effects. *Chin. Phys. B* **2013**, *22*, 114701. [[CrossRef](#)]

27. Mukhopadhyay, S.; Mandal, I.S. Boundary layer flow and heat transfer of a Casson fluid past a symmetric porous wedge with surface heat flux. *Chin. Phys. B* **2014**, *23*, 044702. [[CrossRef](#)]
28. Ariel Hiemenz, P.D. Flow in hydro magnetics. *Acta Mech.* **1994**, *103*, 31–43.
29. Ganapathirao, M.; Ravindran, R. Non-uniform slot suction/injection into mixed convective MHD flow over a vertical wedge with chemical reaction. *Procedia Eng.* **2015**, *127*, 1102–1109. [[CrossRef](#)]
30. Rahman, M.M.; Al-Lawatia, M.A.; Eltayeb, I.A.; Al-Salti, N. Hydromagnetic slip flow of water based nanofluids past a wedge with convective surface in the presence of heat generation (or) absorption. *Int. J. Therm. Sci.* **2012**, *57*, 172–182. [[CrossRef](#)]
31. Srinivasacharya, D.; Mendu, U.; Venumadhav, K. MHD boundary layer flow of a nanofluid past a wedge. *Procedia Eng.* **2015**, *127*, 1064–1070. [[CrossRef](#)]
32. Hammed, H.; Haneef, M.; Shah, Z.; Islam, S.; Khan, W.; Muhammad, S. The Combined Magneto hydrodynamic and electric field effect on an unsteady Maxwell nanofluid Flow over a Stretching Surface under the Influence of Variable Heat and Thermal Radiation. *Appl. Sci.* **2018**, *8*, 160. [[CrossRef](#)]
33. Shah, Z.; Gul, T.; Khan, A.M.; Ali, I.; Islam, S. Effects of hall current on steady three dimensional non-newtonian nanofluid in a rotating frame with brownian motion and thermophoresis effects. *J. Eng. Technol.* **2017**, *6*, 280–296.
34. Shah, Z.; Islam, S.; Gul, T.; Bonyah, E.; Khan, M.A. The electrical MHD and hall current impact on micropolar nanofluid flow between rotating parallel plates. *Results Phys.* **2018**. [[CrossRef](#)]
35. Crane, L.J. Flow past a stretching plate. *Z. Angew. Math. Phys.* **1970**, *21*, 645–647. [[CrossRef](#)]
36. Vajravelu, K.; Roper, T. Flow and heat transfer in a second grade fluid over a stretching sheet. *Int. J. Nonlinear Mech.* **1999**, *34*, 1031–1036. [[CrossRef](#)]
37. Rosca, N.C.; Pop, I. Unsteady boundary layer OW over a permeable curved stretching/shrinking surface. *Eur. J. Mech. B* **2015**, *51*, 61–67. [[CrossRef](#)]
38. Sajid, M.; Ali, N.; Javed, T.; Abbas, Z. Stretching a curved surface in a viscous fluid. *Chin. Phys. Lett.* **2010**, *27*, 024703. [[CrossRef](#)]
39. Khan, W.A.; Pop, I. Boundary-Layer Flow of a Nanouid Past a Stretching Sheet. *Int. J. Heat Mass Transf.* **2010**, *53*, 2477–2483. [[CrossRef](#)]
40. Hassani, M.; Tabar, M.M.; Nemati, H.; Domairry, G.; Noori, F. An analytical solution for boundary layer flow of a Nano liquid past a stretching sheet. *Int. J. Therm. Sci.* **2011**, *50*, 2256–2263. [[CrossRef](#)]
41. Pooya, M.; Rad, C. The Effect of Thermal Radiation on Nanouid Cooled Microchannels. *J. Fusion Energy* **2009**, *28*, 91–100.
42. Afify, A.; Seddeek, M.A.; Bbazid, M.A.A. Radiation effects on Falkner-Skan flow of a nanouid past a wedge in the present of non-uniform heat source/sink. *Meccanica* **2011**, submitted.
43. Brinkman, H.C. The viscosity of concentrated suspensions and solution. *J. Chem. Phys.* **1952**, *20*, 571–581. [[CrossRef](#)]
44. Xue, Q. Model for thermal conductivity of carbon nanotube-based composites. *Phys. B Condens. Matter* **2005**, *368*, 302–307. [[CrossRef](#)]
45. Liao, S.J. On the homotopy analysis method for nonlinear problems. *Appl. Math. Comput.* **2007**, *147*, 499–513. [[CrossRef](#)]
46. Liao, S.J. Comparison between the homotopy analysis method and homotopy perturbation method. *Appl. Math. Comput.* **2005**, *169*, 1186–1194. [[CrossRef](#)]
47. Abbasbandy, S. The application of homotopy analysis method to solve a generalized Hirota-Satsuma Coupled KdV equation. *Phys. Lett. A* **2007**, *361*, 478–483. [[CrossRef](#)]
48. Zhen, W.; Li, Z.; Qing, Z.H. Solitary solution of discrete mKdV equation by homotopy analysis method. *Commun. Theor. Phys.* **2008**, *49*, 1373–1378. [[CrossRef](#)]

